Energy & Environmental Science

ROYAL SOCIETY OF CHEMISTRY

PAPER

View Article Online
View Journal | View Issue

Cite this: *Energy Environ. Sci.*, 2026, **19**, 1680

Electric double layer overlapping effect in high-density sub-nanoclusters for enhanced acidic oxygen evolution reaction

Jiahui Yang,[a] Yixin Hao,[b] Liming Deng,[b] Sung-Fu Hung,[c] Luqi Wang,[b] Gengyu Xing,[b] Feng Hu,[b] Linlin Li,*[b] Tao Wang,*[a] Jianwei Ren,[d] Yuping Wu[a] and Shengjie Peng*[a]

Received 16th November 2025,
Accepted 9th February 2026

DOI: 10.1039/d5ee06950e

rsc.li/ees

The electric double layer (EDL) overlapping between catalyst particles markedly modulates the local surface electric field, yet its influence on acidic oxygen evolution reaction (OER) performance remains elusive. Herein, we construct high-density ruthenium dioxide sub-nanoclusters (RuO_2-SCs) anchored on an amorphous boron–nitrogen–carbon (BNC) support (RuO_2-SCs/BNC) as a model, revealing that EDL overlapping between them elevates the compact layer potential at the catalyst surface. This physical field regulation synergistically enhances the H_3O^+ concentration gradient and boosts intermediate coverage, thereby promoting the formation of the key *OOH intermediate and lowering the energy barrier of the rate-determining step. Concurrently, it stabilizes the Ru–O bonds and markedly mitigates the dissolution of ruthenium active sites. Leveraging these advantages, the catalyst demonstrates exceptional acidic OER performance, with a low overpotential of 142 mV to reach 10 mA cm^{-2} and sustained stability for over 6300 hours. Moreover, it operates stably for 900 hours at 500 mA cm^{-2} in proton exchange membrane water electrolysis. This work elucidates the EDL overlapping regulatory mechanism on acidic OER and provides a novel strategy to synergistically enhance electrocatalyst activity and stability.

Broader context

The development of efficient and stable catalysts for clean energy conversion is crucial for a sustainable future. This work addresses a fundamental challenge in producing green hydrogen through water splitting, which requires highly active and acid-resistant catalysts to facilitate the oxygen evolution reaction. By designing ruthenium oxide sub-nanoclusters at high density on a boron–nitrogen–carbon support, this work exploits a physical phenomenon called "electric double layer overlapping" to enhance both catalytic activity and durability. This approach markedly improves local reactant concentration and stabilizes the catalyst structure under harsh acidic conditions. The resulting material exhibits exceptional performance and longevity, significantly lowering the energy cost of hydrogen production. This study offers a new design principle for electrocatalysts that could accelerate the adoption of large-scale hydrogen energy systems, supporting global efforts in carbon reduction and renewable energy utilization.

Introduction

Although proton exchange membrane water electrolysis (PEMWE) is considered to be a promising technology for converting renewable sources into hydrogen, its large-scale application is constrained by the sluggish kinetics of the anodic oxygen evolution reaction (OER).[1–5] Developing highly efficient and stable acidic OER catalysts is crucial to breaking through this bottleneck. Ruthenium (Ru)-based materials exhibit great potential to replace scarce iridium-based catalysts due to their high intrinsic activity and low cost.[6–9] In current strategies, single-atom Ru catalysts achieve maximum atomic utilization through atomic dispersion but are fundamentally limited by low loadings (<5 wt%),[10,11] preventing attainment of industrial current densities. Isolated atoms are also susceptible to inactivation due to disruption of the coordination environment and dissolution at high oxidation potentials.[12,13] Bulk Ru catalysts, despite their extremely high metal content and thermodynamic stability, suffer from low catalytic efficiency due to extremely limited

[a] *Confucius Energy Storage Lab, School of Energy and Environment & Z Energy Storage Center, Southeast University, Nanjing 211189, China. E-mail: pengshengjie@seu.edu.cn*
[b] *College of Materials Science and Technology, Nanjing University of Aeronautics and Astronautics, Nanjing 210016, China*
[c] *Department of Applied Chemistry, National Yang Ming Chiao Tung University, Hsinchu 300, Taiwan*
[d] *Department of Chemical Engineering, University of Pretoria, Pretoria 0028, South Africa*

utilization, as only surface atoms participate in reactions.[14,15] Their activity is also readily attenuated due to surface passivation, where excessive oxidation triggers a deleterious surface reconstruction that ultimately compromises catalytic performance.[16–18] Sub-nanoclusters (SCs, 1–3 nm in size), as a special structure between single atoms and nanoparticles, retain the advantages of high atom utilization and abundant surficial active sites of single-atom catalysts.[19–21] They also enhance structural stability and metal loading through synergistic interatomic interactions, which provides a novel idea for balancing the activity stability and atom economy of Ru-based catalysts.

Most studies focus on sub-nanocluster size,[22] composition,[23] morphology[24] and metal-carrier charge transfer.[25] However, the effect of Helmholtz layer electron cloud overlapping, which is the electric double layer (EDL) overlapping effect, triggered by neighboring sub-nanocluster spacing smaller than the Debye length (λ_D) in high-density integrated systems on OER catalytic performance, remains unelucidated. Notably, studies on model systems (*e.g.*, nanogap electrodes) have confirmed that EDL overlapping can reconfigure interfacial fields and ion distributions.[26,27] In electrocatalysis, related concepts like "field effects" are often subsumed within complex chemical modifications, leaving the precise physical manipulation of EDL overlapping unexplored, especially for acidic OER.[28] Classical EDL theory indicates that the EDL overlapping effect notably alters the compact layer potential drop (ΔV, $\Delta V = E - V_c$, where E is the electrode potential), which reconfigures interfacial capacitance and reactant adsorption.[27] Previous theory establishes the correlation between adsorption coverage and ΔV, confirming that adsorbate dipole moments on metal surfaces directly modulate compact layer potential distribution.[29,30] This dynamic coupling of ΔV and adsorption coverage strongly suggests that ΔV changes influence the key intermediate concentrations and OER activity. However, studying sub-nanocluster EDL overlapping in electrocatalysis is challenging, as it requires a carrier platform with both high-density cluster anchoring capability and interfacial stability. Notably, boron nitride (BN) offers a stable substrate for sub-nanocluster anchoring, owing to its excellent chemical inertness in acidic media and strong coordination between nitrogen lone pairs and ruthenium d-orbitals.[31] However, the inherent insulation of BN limits charge transfer efficiency in electrocatalysis.[32] Introducing carbon to form a hybrid network not only enhances carrier conductivity but also triggers a unique boron–nitrogen electron compensation effect where electron-deficient boron activates neighboring nitrogen sites, significantly strengthening Ru–N coordination bonds.[33,34] Atomically optimized boron–nitrogen–carbon (BNC) carriers, with unique electronic and structural properties, facilitate stable anchoring of high-density sub-nanoclusters, thus providing an ideal platform for precise regulation of EDL overlapping effects.

In this work, we designed high-density ruthenium dioxide sub-nanoclusters (RuO_2-SCs) anchored on amorphous BNC carriers with abundant anchor points to explore the EDL overlapping effect between sub-nanoclusters for promoting acidic OER. Combined with *in situ* spectroscopy and theoretical calculations, we demonstrate that the EDL overlapping effect can reshape local electric field distribution and compact layer potential through physical field modulation rather than conventional chemical modification. This effect increases the H_3O^+ concentration gradient and intermediate coverage, thereby lowering the energy barrier for rate-determining *OOH formation, stabilizing Ru–O bonds, and inhibiting the dissolution of ruthenium active sites. As a result, the catalyst exhibits a low overpotential of 142 mV at 10 mA cm^{-2} in acidic OER and operates stably for 6300 hours. Moreover, it operates stably for 900 hours at 500 mA cm^{-2} in proton exchange membrane water electrolysis, thus effectively enhancing acidic OER activity and stability. This work not only demonstrates the enhancement mechanism of the EDL overlapping effect on acidic OER but also provides a new approach to synergistically resolve the conflict between OER kinetics and stability.

Results and discussion

Prediction of the EDL overlapping effect on the interfacial regulation

To investigate the EDL overlapping effect of differently distributed sub-nanoclusters and their associated impact on the compact layer potential (V_c), three distinct models were constructed *via* COMSOL Multiphysics simulations. Specifically, RuO_2-SCs with a diameter of 1.4 nm were distributed under three scenarios with edge-to-edge distances (d) of 0.4 nm, 1.4 nm, and 2.4 nm, respectively (Fig. 1a). For larger edge-to-edge distances where d exceeds the Debye length ($d > 2\lambda_D$), the EDLs of sub-nanoclusters do not overlap, and the V_c remains unaffected by neighboring sub-nanoclusters. In this case, owing to the complete Debye shielding of the electric field, the V_c distribution of each sub-nanocluster is equivalent to that of an isolated hemispherical sub-nanocluster. Conversely, for smaller edge-to-edge distances ($d < 2\lambda_D$, λ_D = 0.42 nm), the effect of Debye shielding decreases, and the overlapping of EDLs of neighboring sub-nanoclusters induces significant changes in V_c. Therefore, decreasing the intercluster distance strengthens the EDL overlapping effect, leading to an increase in the V_c on the cluster surface from 69 mV (at d = 2.4 nm) to 148 mV (at d = 1.4 nm), and further to 488 mV (at d = 0.4 nm). Fig. 1b further illustrates the spatial distribution of the ΔV along the arc from the cluster top (point A) to the base (point B). At the smallest distance (d = 0.4 nm), the strong EDL overlapping effect reduces ΔV significantly to a minimum value, with the ΔV at the top A being 131 mV lower than that at the 2.4 nm distance without the EDL overlapping effect, indicating that ΔV is positively correlated with intercluster distance. Furthermore, Frumkin's early research demonstrated that the ΔV within the compact layer of the EDL was proportional to the charge density induced by adsorbed ions.[30,35] Consequently, the reduction in ΔV arising from EDL overlapping influences the charge density of adsorbed ions, which in turn affects their adsorption strength and average coverage.[36]

To evaluate the influence of sub-nanocluster distribution on reactant concentration, we simulated the local H_3O^+ concentration profiles around two cluster models in 0.5 M H_2SO_4

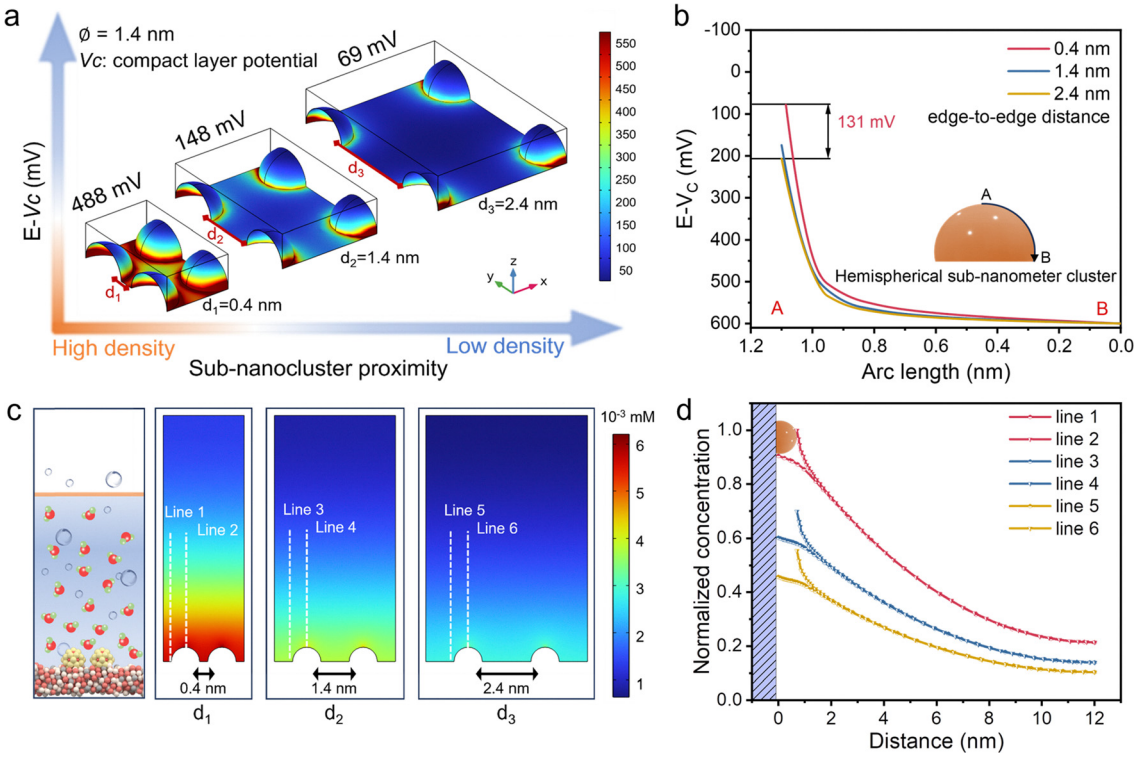

Fig. 1 Simulated microenvironments at different densities of sub-nanoclusters. (a) ΔV and V_c distribution for hemispherical sub-nanoclusters (Φ = 1.4 nm) with intercluster edge-to-edge distances of d = 0.4, 1.4, and 2.4 nm, respectively. (b) ΔV within the compact layer along the arc of the hemispherical sub-nanocluster at various intercluster distances. (c) Simulated steady-state H_3O^+ concentration profile around sub-nanoclusters at various intercluster distances in acid environments. (d) Normalized H_3O^+ concentration at the top and bottom edges of sub-nanoclusters at different intercluster distances, as derived from the simulated results in Fig. 1c. In all simulated cases, a constant potential of 1.4 V is applied at the surfaces of the flat electrode and sub-nanoclusters.

(Fig. 1c), with a focus on the local reactant concentrations at the edges and centers of the nanoclusters, as these sites are typically active for adsorption. The relationship between the local reactant concentrations at the edges and centers and the intercluster distance is presented in Fig. 1d. As the cluster spacing increases from 0.4 nm to 2.4 nm, the H_3O^+ concentrations at the edge and center regions of the RuO_2-SCs decrease by 40% and 55%, respectively. This implies that EDL overlapping can reconfigure the electric field distribution on the cluster surface, which may in turn influence the mass-transfer process of reactants. The reconfigured field can enhance the interfacial transport of charged reactants (H_3O^+) by synergistically promoting both electromigration (directed drift under the electric field) and diffusion (driven by the established concentration gradient), ultimately leading to the observed accumulation of reactants at the interface. Overall, the EDL overlapping in sub-nanometer clusters is of great potential to modulate the surface electric field distribution, elevate the potential of the dense layer, enrich the substrate, enhance mass transfer kinetics, and accelerate the interfacial reaction rate.

Morphological characterization of catalysts

Guided by theoretical predictions, this study developed a two-step strategy to precisely anchor RuO_2-SCs onto an amorphous BNC support, which possesses both high-density cluster anchoring capability and excellent interfacial stability. Briefly, BNC was first synthesized *via* the pyrolysis of boric acid and urea. Subsequently, $RuCl_3$ was mixed with BNC, followed by freeze-drying and calcination. The resultant sample was denoted as RuO_2-SCs/BNC (all the details have been provided in supporting information, [SI]). According to the scanning electron microscopy (SEM) and transmission electron microscopy (TEM) images, the BNC support exhibits a uniform nanotubular structure with an average diameter of approximately 45 nm (Fig. S1 and S2). After anchoring high-density RuO_2-SCs, the BNC support still maintains a well-defined nanotubular morphology (Fig. 2a and Fig. S3). High-resolution transmission electron microscopy (HR-TEM) and spherical aberration corrected transmission electron microscope (AC-TEM) images further present that RuO_2-SCs are uniformly distributed on the BNC support without obvious agglomeration. The average size of each RuO_2-SCs is about 1.4 nm (Fig. 2b–e and Fig. S4), with an edge-to-edge distance of around 0.4 nm (inset of Fig. 2d). Such size and edge-to-edge distance characteristics of sub-nanoclusters provide a structural basis for the occurrence of EDL overlapping. High-angle annular dark-field scanning transmission electron microscopy (HAADF-STEM) and annular bright-field scanning transmission electron microscopy (ABF-STEM) images (Fig. 2f and g) distinguish the atomic distribution between Ru atoms and BNC atoms. The lattice spacing of RuO_2 is 0.25 nm, corresponding to the (101) crystal plane.[37] Energy

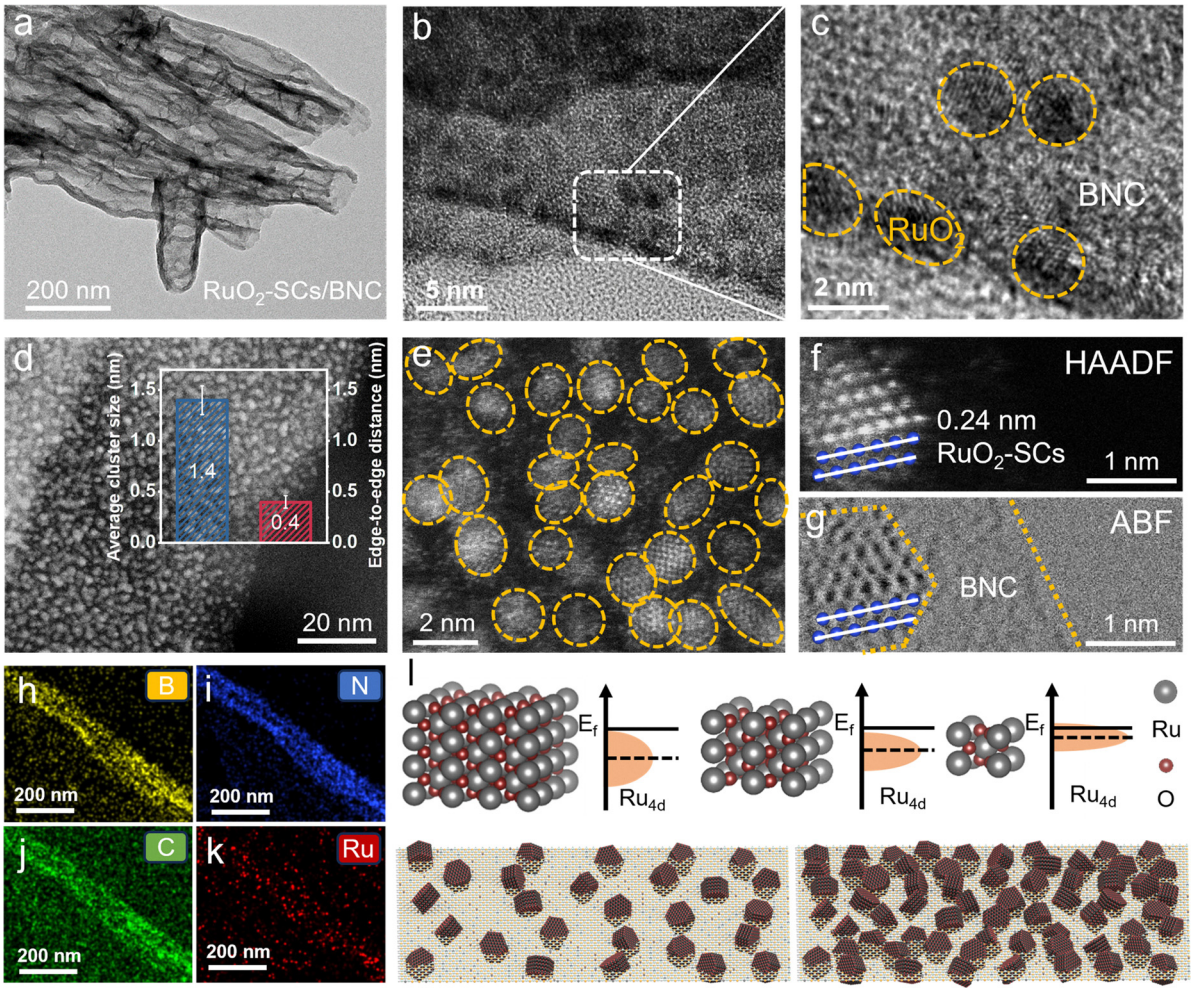

Fig. 2 Morphological Characterizations of RuO_2-SCs/BNC. Bright field (a) TEM and (b) HR-TEM images of RuO_2-SCs/BNC. (c) Enlargement of the selected region in panel b. (d) A dark field TEM image of RuO_2-SCs/BNC. The inset shows the average size and edge-to-edge distance of RuO_2-SCs. (e) AC-TEM image, (f) HAADF-STEM and (g) ABF-STEM images of RuO_2-SCs/BNC. (h–k) B, N, C, and Ru elemental mappings of RuO_2-SCs/BNC. (l) Schematic illustration of how the different sizes and intercluster distances of RuO_2 affect the energy level of the Ru d-bands.

dispersive X-ray (EDX) spectroscopy confirms the uniform distribution of Ru, C, B, and N elements, further verifying the homogeneous dispersion of RuO_2-SCs on the BNC support (Fig. 2h–k). X-ray diffraction (XRD) patterns indicate that the RuO_2-SCs/BNC composite has a crystalline structure consistent with standard RuO_2 (Fig. S5), confirming the successful loading and crystallinity of RuO_2-SCs.

To investigate the influence of the EDL overlapping effect between high-density sub-nanoscale clusters on the electrocatalytic OER of Ru sites, RuO_2 nanoparticles (RuO_2-NPs) were anchored onto the BNC support as a reference sample, which was denoted as RuO_2-NPs/BNC. XRD, SEM, and TEM images show that after being anchored onto the BNC support, the RuO_2-NPs retain a crystalline structure consistent with that of RuO_2, with a uniform particle size of about 10 nm, and are uniformly distributed on the support (Fig. S6–S8). In addition, as measured by inductively coupled plasma optical emission spectrometry (ICP-OES), the RuO_2 content in both RuO_2-SCs/BNC and RuO_2-NPs/BNC is almost the same at 30 wt%. However, as the size of RuO_2 decreases, the packing density increases accordingly, which is beneficial for the subsequent study of the EDL overlapping effect and its influence on OER performance. Generally, a decrease in the particle size of RuO_2 leads to an upshift of the Ru d-band center.[22] In the high-density integrated RuO_2-SCs system constructed in this work, the EDL overlapping effect between neighboring clusters may further modulate the position of the Ru d-band center, thereby laying a robust electronic structure foundation for enhancing the electrocatalytic OER performance (Fig. 2l).

Structure characterization of catalysts

To clarify the chemical structure of RuO_2-SCs/BNC, Fourier transform infrared (FT-IR) spectroscopy was performed (Fig. 3a). The spectrum shows that BNC exhibits a characteristic peak at 1626 cm^{-1}, which is attributed to the bending vibration of C–N bonds. This confirms the successful incorporation of carbon atoms into hexagonal boron nitride (h-BN). After loading RuO_2-SCs, the coupled vibration peak of B-OH/B-NH_2 groups near 3425 cm^{-1} is noticeably enhanced,[38,39] suggesting RuO_2-SCs may

be anchored on BNC *via* N–Ru–O–B bridging structures to facilitate their stable immobilization.[40] X-ray photoelectron spectroscopy (XPS) valence band spectra (VBS) were collected to characterize the band structure properties (Fig. 3b). For the BCN support, it exhibits three characteristic regions, where the low binding energy region (0–3.5 eV) originates from graphitic π-related electrons and N lone-pair electrons, the intermediate region (3.5–11 eV) arises from the superposition of 2p π electrons in C–N, C–B, and N–B bonds, and the high-binding-energy region (11–13 eV) is attributed to σ-bond electrons.[41] Compared with h-BN, BNC shows a significant enhancement of emission intensity within the range of 3.5–13 eV, which can be attributed to the increased density of states (DOS) of pyridine-like C–N structures. This interpretation is further corroborated by density functional theory (DFT) calculations (Fig. S9), which confirm a transition from the wide bandgap of insulating h-BN to a continuous band structure in the conductive BNC matrix. By determining the valence band emission onset to calculate the valence band maximum offset relative to the Fermi level (E_f), the offsets of h-BN and BNC were found to be 1.64 eV and 0.16 eV. This indicates that BNC has a stronger electron transfer capability. After compositing with RuO_2, it can be observed that the 2p π-bond electrons of BNC increase significantly, which resulted from the bonding effect of oxygen atoms. This phenomenon was consistent with the electron paramagnetic resonance (EPR) results (Fig. S11),[42] further confirming that RuO_2-SCs were tightly loaded onto the BNC support through chemical bonding rather than simple physical deposition.

The electronic structure and coordination environment of RuO_2-SCs/BNC and RuO_2-NPs/BNC were further compared. Ultraviolet photoelectron spectroscopy (UPS) measurements revealed that RuO_2-SCs/BNC exhibits a lower work function (6.03 eV) than RuO_2-NPs/BNC (6.71 eV, Fig. 3c). This difference arises from the closely spaced sub-nanoclusters in RuO_2-SCs/BNC, which disrupt the originally continuous metallic valence band and induce the formation of more discrete electronic states. This electronic state transition elevates the E_f and thereby reduces the energy barrier

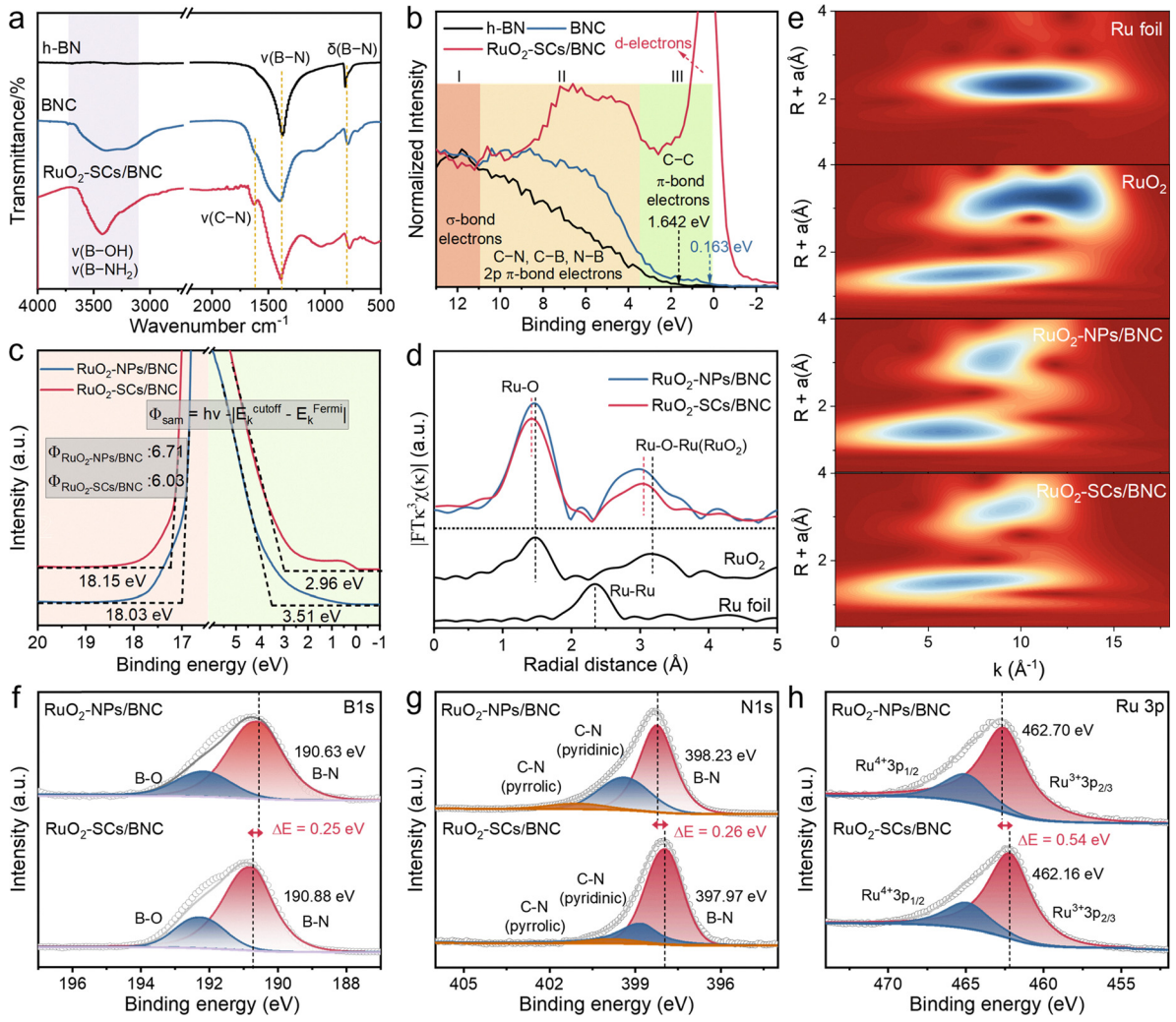

Fig. 3 Structure properties of RuO_2-SCs/BNC and RuO_2-NPs/BNC. (a) FT-IR and (b) XPS valence band spectra of h-BN, BNC and RuO_2-SCs/BNC. (c) UPS spectra of RuO_2-SCs/BNC and RuO_2-NPs/BNC. (d) The Fourier-transform spectra from extended X-ray absorption fine structure (EXAFS) at the Ru K-edge of RuO_2-SCs/BNC, RuO_2-NPs/BNC, RuO_2, and Ru foil in *R*-space. (e) The WT-EXAFS of RuO_2-SCs/BNC, RuO_2-NPs/BNC, RuO_2, and Ru foil at the Ru K-edge. XPS surveys of (f) B 1s, (g) N1s, and (h) Ru 3p for RuO_2-SCs/BNC and RuO_2-NPs/BNC.

for electron emission from the material surface.[43,44] Consequently, the enhanced electron transfer from the catalyst to the antibonding orbitals of adsorbates is favorable for promoting the activation of reactants.[45] The extended X-ray absorption fine structure (EXAFS) spectrum at the Ru edge exhibits two prominent peaks at approximately 1.5 and 3.1 Å (Fig. 3d), corresponding to the nearest Ru–O and subsequent Ru–Ru coordination shells, respectively. Notably, the Ru–O bond length in the sub-nanometer clusters is significantly shortened, arising from the dense packing of high-density RuO_2-SCs. Wavelet transform for EXAFS (WT-EXAFS) further corroborates this observation (Fig. 3e). Additionally, the edge structure of the X-ray absorption near-edge structure (XANES) derivative curve in the 22 080–22 200 eV range reveals that the white line slope of RuO_2-SCs/BNC is lower (Fig. S10). This directly confirms a lower Ru valence state and the formation of a local electron-rich environment at the Ru centers of RuO_2-SCs/BNC. XPS analysis reveals distinct differences in the electronic structures of B, N, and Ru between RuO_2-SCs/BNC and RuO_2-NPs/BNC. Compared with RuO_2-NPs/BNC, the elevated binding energy of B 1s in RuO_2-SCs/BNC indicates that B atoms are in a more electron-deficient state (Fig. 3f), while the reduced binding energy of N 1s suggests an increased electron cloud density around N atoms (Fig. 3g). This phenomenon originates from the interfacial electron transfer within the formed N–Ru–O–B structure and suggests the stronger electronic coupling between RuO_2-SCs and the BNC support. Meanwhile, a pronounced negative shift in the Ru binding energy confirms a higher proportion of Ru^{3+} species in RuO_2-SCs/BNC (Fig. 3h),[46,47] consistent with XANES results. These observations demonstrate that the high-density sub-nanometer clusters effectively optimise the electronic structure of the Ru sites.

Catalyst activity and stability test

The OER activities of RuO_2-SCs/BNC and RuO_2-NPs/BNC were evaluated in 0.5 M H_2SO_4, with commercial RuO_2 and BNC as reference samples. As shown in Fig. 4a, BNC exhibits almost no

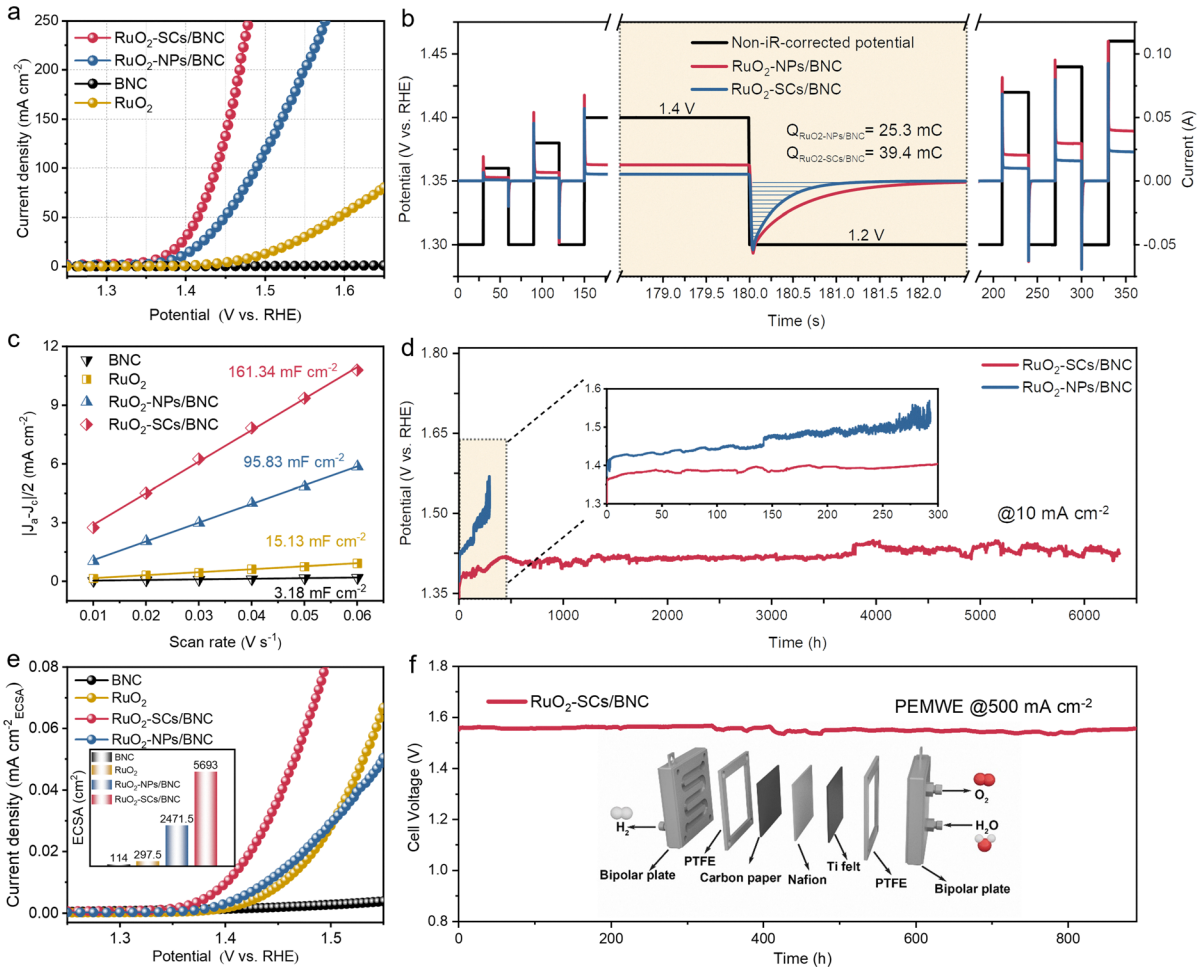

Fig. 4 Electrocatalytic acidic OER performance. (a) LSVs of RuO_2, BNC, RuO_2-NPs/BNC and RuO_2-SCs/BNC conducted at a 5 mV s^{-1} scan rate, in a 0.5 M H_2SO_4 solution with iR correction. (b) Pulse voltammetry protocol curves of RuO_2-NPs/BNC and RuO_2-SCs/BNC. (c) C_{dl} plots of RuO_2, BNC, RuO_2-NPs/BNC and RuO_2-SCs/BNC. (d) Chronopotentiometry test for RuO_2-NPs/BNC and RuO_2-SCs/BNC at 10 mA cm^{-2}. The inset shows a magnified plot of stability in the first 300 hours. (e) ECSA-normalized OER activity of BNC, RuO_2, RuO_2-SCs/BNC and RuO_2-NPs/BNC. The inset shows the detailed ECSA values. (f) PEM device performance (500 mA cm^{-2}) using commercial Pt/C and RuO_2-NPs/BNC as catalysts in the PEM electrolyzer. A schematic of the PEM electrolyzer is shown in the inset, in which the anode and cathode sides are separated by a Nafion membrane.

OER activity, confirming that RuO_2 acts as the primary active site for OER. Compared to RuO_2-NPs/BNC and commercial RuO_2, RuO_2-SCs/BNC shows the lowest OER overpotential of 142 mV at a current density of 10 mA cm^{-2} (Fig. S12), outperforming RuO_2-NPs/BNC (165 mV) and significantly surpassing commercial RuO_2 (258 mV). The faradaic efficiency values of all catalysts were nearly 100%, ensuring that the measured catalytic activities are directly attributable to the intrinsic OER process. (Fig. S13) The corresponding Tafel slope analysis reveals that RuO_2-SCs/BNC (57 mV dec^{-1}) exhibits more favorable reaction kinetics compared to RuO_2-NPs/BNC (61 mV dec^{-1}) and commercial RuO_2 (110 mV dec^{-1}) (Fig. S14).[48] Additionally, RuO_2-SCs/BNC displays an electrochemical double-layer capacitance (C_{dl}) of 161.34 mF cm^{-2}, which is significantly larger than that of the other samples (Fig. 4c and S15). This indicates that high-density sub-nanometer clusters substantially increase the electrochemical active surface area (ECSA) and improve atomic utilization (inset of Fig. 4e), consistent with expectations. Even after normalizing the current density by ECSA, RuO_2-SCs/BNC still maintains significantly higher activity than RuO_2-NPs/BNC and commercial RuO_2 (Fig. 4e). At an overpotential of 200 mV, the normalized current density of RuO_2-SCs/BNC is 0.025 mA cm^{-2}, which is more than three times that of RuO_2-NPs/BNC (0.008 mA cm^{-2}). Additionally, the turnover frequency (TOF) of RuO_2-SCs/BNC is much higher than that of RuO_2 and surpasses most of the most advanced Ru-based catalysts reported in acidic media (Fig. S16). This confirms that RuO_2-SCs/BNC exhibits higher intrinsic catalytic activity.

Pulse voltammetry (PV) was employed to quantify the positive charges accumulated on the electrocatalyst surface. Compared to RuO_2-NPs/BNC, the enhanced peak transient current and accelerated cathodic relaxation of RuO_2-SCs/BNC (Fig. 4b) indicate faster rates of charge accumulation and dissipation, along with enhanced interfacial charge turnover dynamics, thus providing a key kinetic basis for the improved OER activity. Electrochemical impedance spectroscopy (EIS) measurements revealed that RuO_2-SCs/BNC exhibits the smallest charge transfer resistance and efficient electron transfer capability (Fig. S17).[49] Furthermore, *in situ* EIS measurements were performed at various potentials to investigate the interfacial reaction kinetics. As shown in the Bode plots, the phase angle of RuO_2-SCs/BNC in the low-frequency region decreases significantly with increasing potential (Fig. S18 and S19), indicating that the catalyst–electrolyte interface under high-potential conditions is more conducive to rapid electron transfer compared to that of RuO_2-NPs/BNC. This result is attributed to the accelerated surface deprotonation coupled with electron transfer processes, which in turn reduces the activation energy of the OER process.

In addition to catalytic activity, stability under harsh acidic conditions is also critical for evaluating OER catalysts. Chronopotentiometry (CP) tests showed that RuO_2-SCs/BNC operated continuously at a current density of 10 mA cm^{-2} for over 6300 hours during acidic OER. In contrast, the activity of RuO_2-NPs/BNC declined rapidly (Fig. 4d). Notably, the performance of RuO_2-SCs/BNC ranks among the most active Ru-based electrocatalysts reported recently (Table S1). Inductively Coupled Plasma-Mass Spectrometry (ICP-MS) results demonstrated that the concentration of Ru in the solution remained nearly unchanged over the 300-hour stability test, which was significantly lower than the Ru leaching concentration of RuO_2-NPs/BNC (Fig. S20). XPS analyses and TEM characterization after 300 h of electrolysis confirmed the structural stability of RuO_2-SCs/BNC (Fig. S21 and S22). Further, RuO_2-SCs/BNC was utilized as an anodic catalyst for OER and commercial Pt/C as a cathodic catalyst for the hydrogen evolution reaction (HER) to evaluate its potential for practical applications. At 500 mA cm^{-2}, stable operation was maintained for 900 hours, highlighting the significant potential for practical applications (Fig. 4f and Fig. S23). All these results indicate that RuO_2-SCs/BNC possesses not only fast reaction kinetics but also excellent structural and catalytic stability.

In situ characterization of catalysts during OER

In situ XAS was employed to investigate the dynamic evolution of the oxidation state of Ru in the catalyst within the OER potential range. We observed a significant difference in the Ru valence state between RuO_2-SCs/BNC and RuO_2-NPs/BNC, particularly at relatively high applied potentials. When the open-circuit voltage (OCV) was switched from 1.2 V to 1.4 V (*versus* reversible hydrogen electrode, RHE), the average Ru valence states of both RuO_2-SCs/BNC and RuO_2-NPs/BNC exhibited a slight increase. This phenomenon arises because this stage corresponds to the pre-catalysis period during which surface charges accumulate continuously while electrons fail to initiate the electron cycle for water oxidation. It belongs to the oxidation stage of the catalyst, thus manifesting a minor elevation in the oxidation state. As the applied potential was increased from 1.4 V to 2.0 V, the most prominent feature of RuO_2-NPs/BNC was that its Ru valence state increased to +4.1. In contrast, RuO_2-SCs/BNC showed no obvious change and maintained a Ru valence state of approximately +3.98 (Fig. 5d and Fig. S24). This distinction can be attributed to the fact that Ru sites in the sub-nanoclusters are more prone to acquiring electrons from the BNC support. By transferring electrons to Ru species, the catalyst sustains stable catalytic performance and thereby protects the active sites from dissolution under high potentials. This observation accounts for the more remarkable catalytic activity of RuO_2-SCs/BNC compared to RuO_2-NPs/BNC. When the applied potential was returned to OCV, the Ru oxidation state of RuO_2-SCs/BNC decreased again from +3.98 to around +3.93. However, RuO_2-NPs/BNC was unable to revert to its initial valence state and instead exhibited a higher oxidation state. This stage demonstrates that the EDL overlapping effect induced by high-density clusters is beneficial for maintaining the stability of Ru species.

Analysis of the *R*-space information derived from FT-EXAFS visually reveals the evolution of the local Ru–O structure during the OER process. The results demonstrate that the Ru–O bond distance of RuO_2-SCs/BNC does not exhibit obvious changes, whereas the Ru–O bond distance of RuO_2-NPs/BNC increases with the elevation of applied potential. This distinct difference arises from the overlapping electric field generated by high-density clusters, which stabilizes the Ru sites and suppresses the formation of amorphous layers. Meanwhile, the Ru–O coordination number of

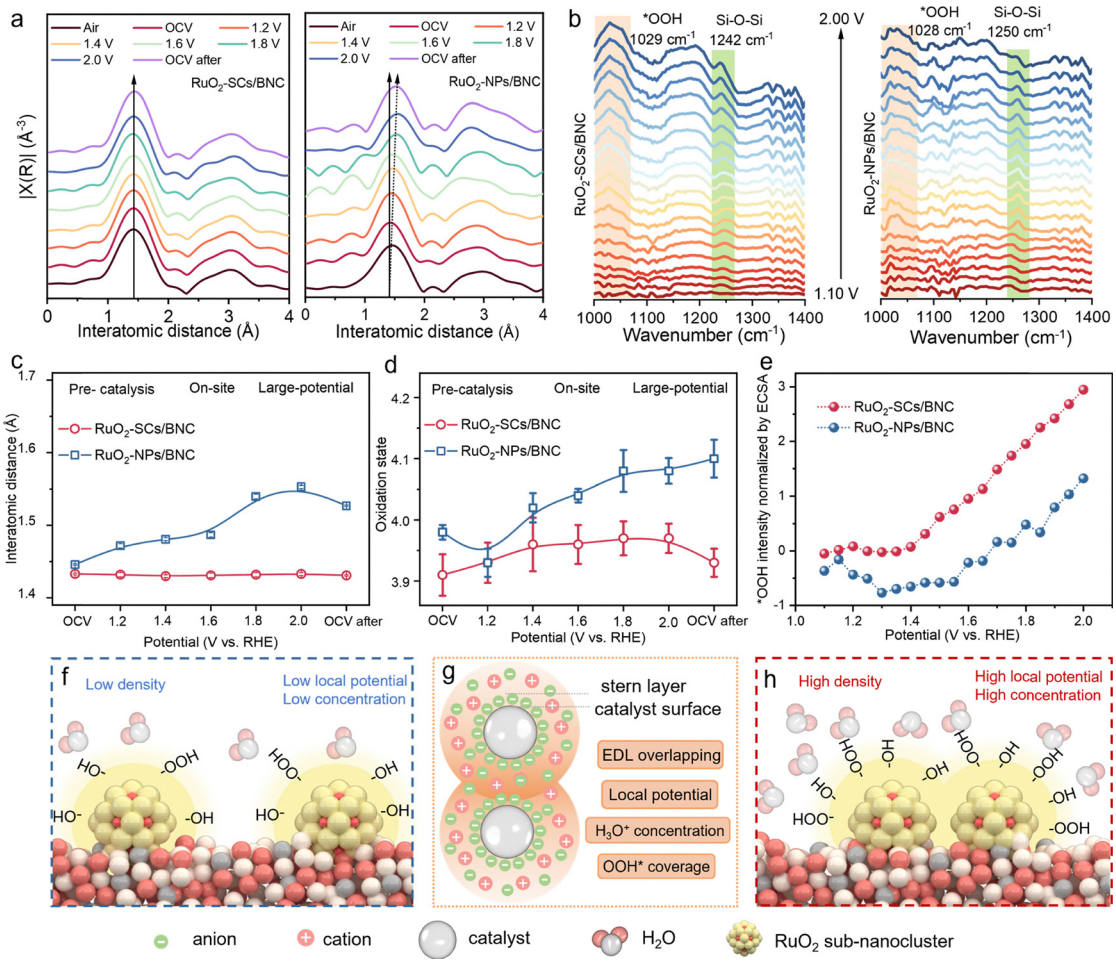

Fig. 5 Investigating the structure evolution during OER. (a) Operando FT-EXAFS for Ru K-edge of RuO_2-SCs/BNC (left panel) and RuO_2-NPs/BNC (right panel). (b) *In situ* FTIR spectra of RuO_2-SCs/BNC (left panel) and RuO_2-NPs/BNC (right panel) in the range of 1000–1400 cm^{-1} at different applied potentials. (c) Summary of the Ru-O interatomic distance of RuO_2-SCs/BNC and RuO_2-NPs/BNC at various potentials. (d) The valence states of RuO_2-SCs/BNC and RuO_2-NPs/BNC fitted by Ru K-edge absorption energy at different potentials. (e) Summary of the *OOH intensity of RuO_2-SCs/BNC and RuO_2-NPs/BNC normalized by ECSA at various potentials. (f) Schematic representation of the electrochemical interface of RuO_2-NPs/BNC. (g) Schematic illustration of the EDL overlapping in RuO_2-SCs. (h) Schematic representation of the electrochemical interface of RuO_2-SCs/BNC during water oxidation.

RuO_2-NPs/BNC decreases slightly, and this phenomenon is attributed to the generation of oxygen vacancies and structural damage (Fig. 5a and c). This was corroborated by WT-EXAFS (Fig. S25 and S26).

In summary, the high-density structure plays a crucial role in enabling the high OER activity of the Ru–O moiety. Additionally, the introduced BNC mitigates the limitations associated with the electron transfer and reactant mass transport, then enhancing behavior of reaction intermediates on electrocatalyst surfaces. The methanol oxidation reaction (MOR) was employed as a probe reaction to evaluate the coverage of *OH intermediates on the catalyst surface. Methanol molecules readily undergo nucleophilic attack by electrophilic *OH species (Fig. S27c), thus exhibiting enhanced oxidative activity on surfaces with stronger *OH adsorption.[50] By introducing 0.1 M methanol into the electrolyte, the current density difference contributed by MOR can be quantified through the area integration between the MOR and OER polarization curves, where this difference is proportional to the transferred charge. Compared with RuO_2-NPs/BNC, RuO_2-SCs/BNC demonstrates stronger competitive reactivity in MOR, indicating a significantly enhanced surface *OH adsorption capacity (Fig. S27a, b and S28).

In situ ATR-SEIRAS spectroscopy was employed to further identify the reaction intermediates. For both RuO_2-SCs/BNC and RuO_2-NPs/BNC, distinct absorption bands were observed at 1028 cm^{-1} and 1029 cm^{-1}, respectively. These bands are attributed to the stretching vibration of *OOH, a key intermediate in the OER (Fig. 5b). This observation indicates that the OER process over both RuO_2-SCs/BNC and RuO_2-NPs/BNC is dominated by the adsorbate evolution mechanism (AEM, Fig. S29) rather than the lattice oxygen-mediated mechanism (LOM).[51] The AEM reaction pathway prevents lattice oxygen in LOM from participating in the reaction. This prevention inhibits the dissolution of the catalyst and thereby enhances the catalyst stability. When the intensity normalized by ECSA, the *OOH coverage on RuO_2-SCs/BNC surface was found to be twice that on RuO_2-NPs/BNC

(Fig. 5e and Fig. S30). This result arises from the EDL overlapping effect induced by the high arrangement of RuO_2-SCs, which elevates the potential of the compact layer (Fig. S31), promotes the adsorption and activation of water molecules, accelerates their dissociation to generate OH intermediates, drives the enrichment of OH intermediates on Ru active sites, and further facilitates the formation of the key *OOH intermediate. This is also consistent with the previous theoretical simulations, which indicate that the EDL overlapping effect facilitates the enrichment of a higher H_3O^+ concentration on the surface of high-density clusters, thereby increasing the coverage of OH and *OOH intermediates and further enhancing the OER kinetics (Fig. 5f–h).

DFT calculation of oxygen evolution mechanism

The core steps of AEM include the adsorption of two water molecules, dehydrogenation, and the final formation of the key *OOH intermediate (Fig. 6a).[52] The generation of this intermediate directly completes the formation of the O–O bond, so this bond formation is a core step for efficient oxygen evolution. Promoting the formation of *OOH is therefore crucial for improving the OER efficiency. To gain deeper insights into why high-density RuO_2 clusters loaded on BNC (H-RuO_2/BNC) exhibit higher catalytic activity than high-density RuO_2 loaded on BNC (L-RuO_2/BNC), DFT calculations were performed to evaluate the Gibbs free energy of the four-step reaction in AEM. The results show that the rate-determining step (RDS) for both samples is the formation of *OOH (Fig. 6b and Fig. S32–S34). The energy barrier of this step on the H-RuO_2/BNC surface is relatively low (1.71 eV). This value is significantly lower than the energy barrier on the L-RuO_2/BNC surface (1.97 eV), thus effectively reducing the energy barrier of the RDS. Furthermore, as shown in the DOS plot in Fig. 6c, the d-band center of Ru in H-RuO_2/BNC (−0.83 eV) exhibits a significant negative shift compared with that in L-RuO_2/BNC (−0.78 eV). This originates from the formation of a localized and enhanced electrostatic field at the interface of H-RuO_2/BNC, which is induced by the EDL overlapping between neighboring RuO_2 clusters. This strong electrostatic field acts as an effective electron modulator, polarizing and redistributing the electron cloud of the RuO_2. This redistribution ultimately leads to the negative shift of the Ru d-band center, which in turn optimizes the adsorption strength of active sites toward oxygen-containing intermediates, significantly reduces the energy barrier for *OOH formation, and thus enables H-RuO_2/BNC to exhibit excellent oxygen OER activity.

To further elucidate the mechanism underlying the enhanced catalyst stability, demetallation and lattice oxygen removal energies of Ru in acidic environments were calculated (Fig. 6d). H-RuO_2/BNC exhibits the highest Ru demetallation energy (2.54 eV), significantly higher than that of RuO_2-NPs/BNC (1.52 eV) and L-RuO_2-/BNC (1.88 eV). It also exhibits the highest lattice oxygen removal energy (3.77 eV), much higher than that of RuO_2-NPs/BNC (2.56 eV) and L-RuO_2/BNC (3.26 eV). The enhanced stability of H-RuO_2/BNC originates from the redistribution and delocalization of interfacial electrons, which ensures a highly efficient electron supply throughout the reaction. Bader charge analysis results further confirm this (Fig. S35). They indicate that the electron transfer from the BNC support to RuO_2 clusters is most significant in H-RuO_2/BNC. The enhanced interfacial electron interaction effectively stabilizes the Ru–O bonds. Therefore, the significantly increased dissolution energy and lattice oxygen removal energy indicate that H-RuO_2/BNC has stronger resistance to solvation erosion. This essentially enhances its structural stability under acidic OER conditions.

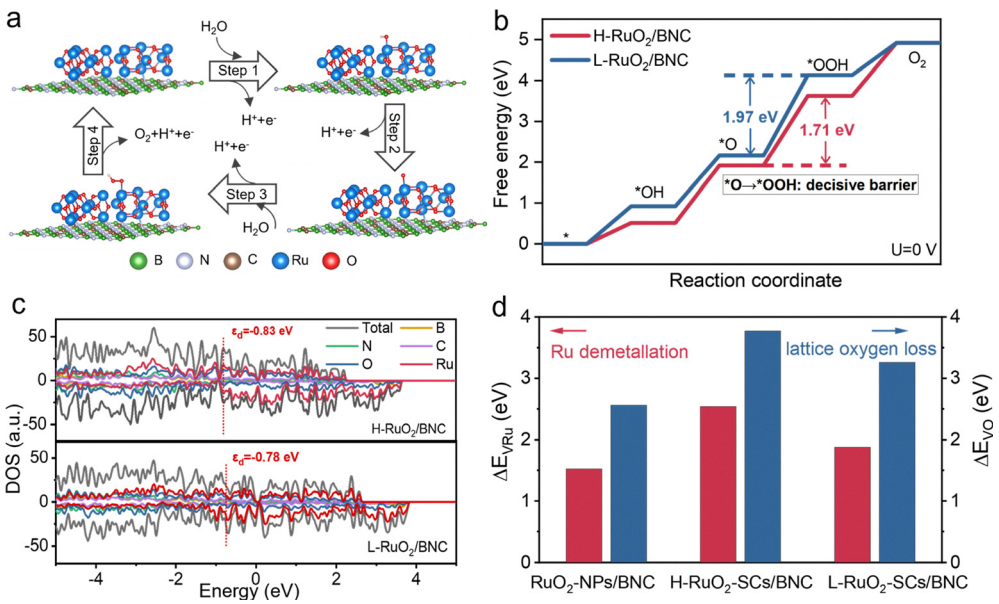

Fig. 6 DFT calculations on high/low-density RuO_2-SCs on BNC. (a) Schematic illustration of high and low-density RuO_2-SCs on BNC. (b) The OER free energy diagrams on simulated H/L-RuO_2/BNC. (c) DOS patterns for the corresponding B, N, C, O and Ru of H-RuO_2-SCs/BNC and L-RuO_2-SCs/BNC. (d) Calculated energies of Ru demetallation and lattice oxygen loss for RuO_2-NPs/BNC, H-RuO_2-SCs/BNC and L-RuO_2-SCs/BNC during the OER reaction.

Conclusions

In summary, by constructing a high-density spatial array of RuO_2-SCs on a BNC support, we investigated the impact of the EDL overlapping effect on the acidic OER. This EDL overlapping effect optimized the interfacial potential distribution, specifically elevating the compact layer potential, and enhanced the H_3O^+ concentration gradient by 55%. These changes accelerated *OH generation, doubled the coverage of the critical *OOH intermediate, and reduced the *OOH formation energy barrier by 0.26 eV. Concurrently, the localized electric field stabilized Ru–O bonds, increased the dissolution energy barrier, and effectively suppressed over-oxidation of active sites. As a result, the RuO_2-SCs/BNC catalyst achieved a low overpotential of 142 mV at 10 mA cm^{-2}, maintained stability for 6300 hours in acidic OER, and even operated stably for 900 hours at 500 mA cm^{-2} in PEMWE. This work provides a novel insight into synergistically breaking the activity–stability trade-off of RuO_2-based catalysts in acidic OER.

Author contributions

The manuscript was written through the contributions of all authors. All authors have given approval to the final version of the manuscript.

Conflicts of interest

The authors declare no competing financial interest.

Data availability

The data that support the findings of this study are available from the corresponding author upon reasonable request. Supplementary information (SI) is available. See DOI: https://doi.org/10.1039/d5ee06950e.

Acknowledgements

This work was supported by the National Natural Science Foundation of China (52371226, 92472117, and 22402081), and the Natural Science Foundation of Jiangsu Province (BK20221482 and BK20210311).

References

1 R.-T. Liu, Z.-L. Xu, F.-M. Li, F.-Y. Chen, J.-Y. Yu, Y. Yan, Y. Chen and B. Y. Xia, *Chem. Soc. Rev.*, 2023, **52**, 5652.
2 H. B. Tao, H. Liu, K. Lao, Y. Pan, Y. Tao, L. Wen and N. Zheng, *Nat. Nanotechnol.*, 2024, **19**, 1074.
3 R. Wan, T. Yuan, L. Wang, B. Li, M. Liu and B. Zhao, *Nat. Catal.*, 2024, **7**, 1288–1304.
4 W. Shi, T. Shen, C. Xing, K. Sun, Q. Yan, W. Niu, X. Yang, J. Li, C. Wei, R. Wang, S. Fu, Y. Yang, L. Xue, J. Chen, S. Cui, X. Hu, K. Xie, X. Xu, S. Duan, Y. Xu and B. Zhang, *Science*, 2025, **387**, 791–796.
5 Y. Song, H. Chen, X. Wang, C. Weng, K. Zou, C. Wang, Y. Yuan, Y. Ma, X. Yang and W. Lin, *Energy Environ. Sci.*, 2025, **18**, 130–154.
6 Y. Wang, H. Yan and H. Fu, *eScience*, 2025, **5**, 100323.
7 W. Li, C. Wang and X. Lu, *Nano Lett.*, 2024, **24**, 11779–11792.
8 S. Li, S. Zhao, F. Hu, L. Li, J. Ren, L. Jiao, S. Ramakrishna and S. Peng, *Prog. Mater. Sci.*, 2024, **145**, 101294.
9 K. Wang, Y. Wang, B. Yang, Z. Li, X. Qin, Q. Zhang, L. Lei, M. Qiu, G. Wu and Y. Hou, *Energy Environ. Sci.*, 2022, **15**, 2356–2365.
10 H. Zhang, J. Wang, J. Yao, Q. Yang, X. Zuo, H. Tang, W. Wang, L. Yang and G. Li, *Angew. Chem., Int. Ed.*, 2025, e202506563.
11 Z. Zhang, P. Ma, C. Jia, W. Gao, M. Liu, K. N. Hui, M. Zuo, S. Zhou and J. Zeng, *eScience*, 2025, 100402.
12 J. Liu, J. Yang, Y. Dou, X. Liu, S. Chen and D. Wang, *Adv. Mater.*, 2025, **37**, 2420383.
13 Y. Cui, C. Ren, M. Wu, Y. Chen, Q. Li, C. Ling and J. Wang, *J. Am. Chem. Soc.*, 2024, **146**, 29169–29176.
14 M. Peng, C. Dong, R. Gao, D. Xiao, H. Liu and D. Ma, *ACS Cent. Sci.*, 2021, 7, 262–273.
15 G. Luo, M. Song, Q. Zhang, L. An, T. Shen, S. Wang, H. Hu, X. Huang and D. Wang, *Nano-Micro Lett.*, 2024, **16**, 241.
16 Z.-Y. Wu, F.-Y. Chen, B. Li, S.-W. Yu, Y. Z. Finfrock, D. M. Meira, Q.-Q. Yan, P. Zhu, M.-X. Chen, T.-W. Song, Z. Yin, H.-W. Liang, S. Zhang, G. Wang and H. Wang, *Nat. Mater.*, 2023, **22**, 100–108.
17 J. Zhang, X. Fu, S. Kwon, K. Chen, X. Liu, J. Yang, H. Sun, Y. Wang, T. Uchiyama, Y. Uchimoto, S. Li, Y. Li, X. Fan, G. Chen, F. Xia, J. Wu, Y. Li, Q. Yue, L. Qiao, D. Su, H. Zhou, W. A. Goddard and Y. Kang, *Science*, 2025, **387**, 48–55.
18 W. Li, D. Chen, Z. Lou, H. Yuan, X. Fu, H. Y. Lin, M. Lin, Y. Hou, H. Qi, P. F. Liu, H. G. Yang and H. Wang, *J. Am. Chem. Soc.*, 2025, **147**, 10446–10458.
19 Y. Deng, Y. Guo, Z. Jia, J.-C. Liu, J. Guo, X. Cai, C. Dong, M. Wang, C. Li, J. Diao, Z. Jiang, J. Xie, N. Wang, H. Xiao, B. Xu, H. Zhang, H. Liu, J. Li and D. Ma, *J. Am. Chem. Soc.*, 2022, **144**, 3535–3542.
20 Q. Liu and X. Wang, *Chem. Catal.*, 2022, **2**, 1257–1266.
21 L. Wan, H. Wang, B. Zeng, W. Wang, X. Liu, L. Cao, Y. Hu, Z. Cui and B. Dong, *Energy Environ. Sci.*, 2025, **18**, 4262–4275.
22 Q. Hu, K. Gao, X. Wang, H. Zheng, J. Cao, L. Mi, Q. Huo, H. Yang, J. Liu and C. He, *Nat. Commun.*, 2022, **13**, 3958.
23 L. Liu and A. Corma, *Chem. Rev.*, 2023, **123**, 4855–4933.
24 B. Ni, Y. Shi and X. Wang, *Adv. Mater.*, 2018, **30**, 1802031.
25 C. Pan, C. Wang, X. Zhao, P. Xu, F. Mao, J. Yang, Y. Zhu, R. Yu, S. Xiao, Y. Fang, H. Deng, Z. Luo, J. Wu, J. Li, S. Liu, S. Xiao, L. Zhang and Y. Guo, *J. Am. Chem. Soc.*, 2022, **144**, 4942–4951.
26 Y. Ma, L.-H. Yeh, C.-Y. Lin, L. Mei and S. Qian, *Anal. Chem.*, 2015, **87**, 4508–4514.
27 H. C. Lee, J. Kim, H. J. Yang, J. Yu and J. H. Bae, *Anal. Chem.*, 2024, **96**, 18745–18753.
28 J. Zhou, W. Nie, D. E. Tarnopol and C. C. L. McCrory, *Chem. Catal.*, 2024, **4**, 101006.
29 X. Shi, J. Xie, F. Yang, F. Wang, D. Zheng, X. Cao, Y. Yu, Q. Liu and X. Lu, *Angew. Chem., Int. Ed.*, 2022, **61**, e202214773.

30 O. Stern, *Z. Elektrochem. Angew. Phys. Chem.*, 1924, **30**, 508.
31 M. Xu, T. Liang, M. Shi and H. Chen, *Chem. Rev.*, 2013, **113**, 3766–3798.
32 G. Postole, A. Gervasini, M. Caldararu, B. Bonnetot and A. Auroux, *Appl. Catal., A*, 2007, **325**, 227–236.
33 X. Zhang, J. Deng, T. Lan, Y. Shen, Q. Zhong, W. Ren and D. Zhang, *ACS Catal.*, 2022, **12**, 14152–14161.
34 Z. Song, Z. Li, H. Wang, X. Bai, W. Wang, H. Du, S. Liu, C. Wang, J. Han, Y. Yang, Z. Liu, J. Lu, Z. Fang and J. Yang, *Nano Lett.*, 2017, **17**, 2079–2087.
35 H. Gerischer, *Interscience*, 1966, **70**, 765.
36 M. Nesselberger, M. Roefzaad, R. Fayçal Hamou, P. Ulrich Biedermann, F. F. Schweinberger, S. Kunz, K. Schloegl, G. K. H. Wiberg, S. Ashton, U. Heiz, K. J. J. Mayrhofer and M. Arenz, *Nat. Mater.*, 2013, **12**, 919.
37 Y. Xue, J. Zhao, L. Huang, Y.-R. Lu, A. Malek, G. Gao, Z. Zhuang, D. Wang, C. T. Yavuz and X. Lu, *Nat. Commun.*, 2023, **14**, 8093.
38 L. Yang, J. Guo and L. Zhang, *Polymer*, 2023, **280**, 126016.
39 W. Lei, V. N. Mochalin, D. Liu, S. Qin, Y. Gogotsi and Y. Chen, *Nat. Commun.*, 2015, **6**, 8849.
40 Y. Hao, S.-F. Hung, C. Tian, L. Wang, Y.-Y. Chen, S. Zhao, K.-S. Peng, C. Zhang, Y. Zhang, C.-H. Kuo, H.-Y. Chen and S. Peng, *Angew. Chem., Int. Ed.*, 2024, **63**, e202402018.
41 C. Huang, C. Chen, M. Zhang, L. Lin, X. Ye, S. Lin, M. Antonietti and X. Wang, *Nat. Commun.*, 2015, **6**, 7698.
42 Y. Tian, M. Yang and C. Wang, *J. Mater. Chem. A*, 2022, **10**, 8826–8836.
43 C. Wang, H. Lu, Z. Mao, C. Yan, G. Shen and X. Wang, *Adv. Funct. Mater.*, 2020, **30**, 2000556.
44 S. Zhao, S.-F. Hung, L. Deng, W.-J. Zeng, T. Xiao, S. Li, C.-H. Kuo, H.-Y. Chen, F. Hu and S. Peng, *Nat. Commun.*, 2024, **15**, 2728.
45 Z. Chen, X. Li, H. Ma, Y. Zhang, J. Peng, T. Ma, Z. Cheng, J. Gracia, Y. Sun and Z. J. Xu, *Natl. Sci. Rev.*, 2024, **11**, nwae314.
46 Q. He, Y. Zhou, H. Shou, X. Wang, P. Zhang, W. Xu, S. Qiao, C. Wu, H. Liu, D. Liu, S. Chen, R. Long, Z. Qi, X. Wu and L. Song, *Adv. Mater.*, 2022, **34**, 2110604.
47 Z. Chen, X. Dong, Z.-X. Sun, X. An, C. Li, S. Liu, J. Shen, C. Wu, J. Wang, Z. Wang, Z. Zhu, Y. Zhou, K. Yu, Y. Ma, J. He, K. Feng, L. He and Z. Hu, *ACS Nano*, 2024, **18**, 19672–19681.
48 A. Grimaud, O. Diaz-Morales, B. Han, W. T. Hong, Y.-L. Lee, L. Giordano, K. A. Stoerzinger, M. T. M. Koper and Y. Shao-Horn, *Nat. Chem.*, 2017, **9**, 457–465.
49 W. Li, J. Lv, X. Chen, B. Wang and L. Wang, *J. Am. Chem. Soc.*, 2025, **147**, 29505–29516.
50 H. B. Tao, Y. Xu, X. Huang, J. Chen, L. Pei, J. Zhang, J. G. Chen and B. Liu, *Joule*, 2019, **3**, 1498–1509.
51 Y. Pan, X. Xu, Y. Zhong, L. Ge, Y. Chen, J.-P. M. Veder, D. Guan, R. O'Hayre, M. Li, G. Wang, H. Wang, W. Zhou and Z. Shao, *Nat. Commun.*, 2020, **11**, 2002.
52 X. Ping, Y. Liu, L. Zheng, Y. Song, L. Guo, S. Chen and Z. Wei, *Nat. Commun.*, 2024, **15**, 2501.

